An EPID-based method to determine mechanical deformations in a linear accelerator

Daniel Gourdeau
Département de Radio-Oncologie, CHU de Québec, 11 Côte du Palais, Québec, QC, Canada, G1R 0A2
Département de Physique, de Génie physique et d'Optique, Université Laval, 2325 rue de l' Université, Québec, QC, Canada, G1V 0A6

Luc Gingras, Frédéric Beaulieu, and Ghyslain Leclerc
Département de Radio-Oncologie, CHU de Québec, 11 Côte du Palais, Québec, QC, Canada, G1R 0A2

Louis Archambault[a)]
Département de Radio-Oncologie, CHU de Québec, 11 Côte du Palais, Québec, QC, Canada, G1R 0A2
Département de Physique, de Génie physique et d'Optique, Université Laval, 2325 rue de l' Université, Québec, QC, Canada, G1V 0A6

(Received 4 October 2017; revised 19 July 2018; accepted for publication 5 September 2018; published xx xxxx xxxx)

Purpose: Medical linear accelerators (linac) are delivering increasingly complex treatments using modern techniques in radiation therapy. Complete and precise mechanical QA of the linac is therefore necessary to ensure that there is no unexpected deviation from the gantry's planned course. However, state-of-the-art EPID-based mechanical QA procedures often neglect some degrees of freedom (DOF) like the in-plane rotations of the gantry and imager or the source movements inside the gantry head. Therefore, the purpose of this work is to characterize a 14 DOF method for the mechanical QA of linacs. This method seeks to measure every mechanical deformation in a linac, including source movements, in addition to relevant clinical parameters like mechanical and radiation isocenters.

Methods: A widely available commercial phantom and a custom-made accessory inserted in the linac's interface mount are imaged using the electronic portal imaging device (EPID) at multiple gantry angles. Then, simulated images are generated using the nominal geometry of the linac and digitized models of the phantoms. The nominal geometry used to generate these images can be modified using 14 DOF (3 rigid rotations and 3 translations for the imager and the gantry, and 2 in-plane translations of the source) and any change will modify the simulated image. The set of mechanical deformations that minimizes the differences between the simulated and measured image is found using a genetic algorithm coupled with a gradient-descent optimizer. Phantom mispositioning and gantry angular offset were subsequently calculated and extracted from the results. Simulations of the performances of the method for different levels of noise in the phantom models were performed to calculate the absolute uncertainty of the measured mechanical deformations. The measured source positions and the center of collimation were used to define the beam central axis and calculate the radiation isocenter position and radius.

Results: After the simultaneous optimization of the 14 DOF, the average distance between the center of the measured and simulated ball bearings on the imager was 0.086 mm. Over the course of a full counter-clockwise gantry rotation, all mechanical deformations were measured, showing sub-millimeter translations and rotations smaller than 1° along every axis. The average absolute uncertainty of the 14 DOF (1 SD) was 0.15 mm or degree. Phantom positioning errors were determined with more than 0.1 mm precision. Errors introduced in the experimental setup like phantom positioning errors, source movements or gantry angular offsets were all successfully detected by our QA method. The mechanical deformations measured are shown to be reproducible over the course of a few weeks and are not sensitive to the experimental setup.

Conclusion: This work presents of new method for an accurate mechanical QA of the linacs. It features a 14 DOF model of the mechanical deformations that is both more complete and precise than other available methods. It has demonstrated sub-millimeter accuracy through simulation and experimentation. Introduced errors were successfully detected with high precision. © *2018 American Association of Physicists in Medicine* [https://doi.org/10.1002/mp.13184]

Key words: geometric calibration, isocenter check, linear accelerator, radiation therapy

1. INTRODUCTION

Modern techniques in radiation therapy like volumetric arc therapy (VMAT) or stereotactic radiosurgery place heavy requirements on the mechanical accuracy of the treatment system. Nevertheless, over the course of its full rotation around a patient, the gantry head deviates from its planned course due to gravity, eccentricity of gantry rotation or mechanical imperfections. Mechanical quality assurance (QA) of the linac is therefore essential to guarantee a good treatment outcome,[1] by monitoring those deformations and correcting or mitigating them. Another critical element of the linear accelerator is the electronic portal imaging device (EPID), which has been widely used for QA tests. EPIDs are also affected by mechanical deviations, which can lead to positioning errors if left uncorrected. Simple models have been used to measure and correct those mechanical deformations, taking into account only the in-plane and cross-plane translations of the EPID and gantry. More sophisticated ones also measure changes in distance between the radiation source and the imager to account for scaling, and in-plane rotation of the imager. Rowshanfarzad et al.[2] also introduced a 8 degrees of freedom (DOF) method which measured every rotation of the imager. Another 8 DOF approach to geometric quality assurance is the work by Mao et al.[3,4] that introduced the gQA phantom that characterize source position and imager deformations for both MV and kV imaging. The long-term stability and accuracy of this system has already been evaluated.[5] However, some DOF in the system are neglected. Indeed, gantry rotations around every axis should be measured. It has also been shown that the radiation source can be slightly displaced relative to the primary collimator of the treatment head,[6] which should be taken into account. Therefore, the purpose of this work is to design and develop a method for 14 DOF mechanical QA of linear accelerators. The additional degrees of freedom should provide more accurate measurements and a very exhaustive testing of the mechanical properties of the linear accelerator. The principles of the method are laid out in this work and a proof-of-concept is established through simulation. The expected performances of the system are also characterized. Finally, we review results of this test that have been performed on actual linacs in different situations.

2. MATERIALS AND METHOD

The proposed QA procedure requires: (a) a phantom containing a set of markers placed on the treatment couch and roughly aligned with the room lasers; (b) a custom accessory with markers placed in the fixed interface mount of the gantry. The presence of the accessory in the interface mount is necessary in order to help distinguish a gantry movement from an imager movement on the image. Other works focusing on linac mechanical QA also use markers that are fixed relative to the head of the gantry for similar reasons.[2,7] In this work, the chosen phantom was the Isocal phantom from Varian, but other commercial or custom phantoms could be used to the same effect. The IsoCal phantom is composed of 16 tungsten-carbide ball bearings (BBs) with diameters of 4 mm spread over a large cylindrical plastic phantom with a hollow center. It is being used routinely at our center in the manner presented by Mamalui-Hunter.[7] The accessory for the interface mount is a custom made acrylic plate with 16 BBs with diameters of 4 mm drilled and fixed on it. It was designed so that the projection of the rigidly-attached BBs would not overlap with the projection of the BBs of the IsoCal phantom at specific gantry and collimator angles. The minimum separation on the image between each BBs centers was set at 8 mm. The choice of the IsoCal phantom has been driven mostly by its widespread availability. Any other phantom with a sufficient number of BBs could also be used, provided that a suitable model is available and that the accessory's BBs don't overlap with it at the desired gantry angles. A Varian TrueBeam medical linear accelerator (Varian medical systems, Palo Alto, CA) is used to perform the irradiation and the aS1200 EPID with pixel size 0.336×0.336 mm^2 is used to acquire images that are subsequently exported and saved as DICOM RT images. The BB's positions on the EPID image are extracted using circle Hough transform (CHT). Inaccurate BB detection is handled with automated warnings if the distance between the expected position and the measured position exceeds a given threshold (5 mm). This threshold is kept rather large to account for possible phantom mispositioning. However, it is small enough to identify CHT artifacts due to incorrect edge detection. However, CHT artifacts were greatly reduced after adding some image pre-processing steps before CHT. Images are pre-processed by extracting the intensity gradient due to the attenuation of the phantom, which can prevent good CHT detection. This is done by applying anisotropic gaussian blurring in the inplane direction to preserve the crossplane gradient and smooth out the BBs. The smoothed image is then subtracted from the original image. The phantom is irradiated using a 25×20 cm^2 field defined by the multileaf collimator (MLC) with the EPID placed at 1500 mm source-detector distance (SDD). Measurements are then repeated for 16 uniformly spaced gantry angles. At each gantry angle, every BBs are visible in the field of view, for a constant number of 32 objects being imaged.

2.A. Modelisation

A program has been written in C++ to model the mechanical behavior of a linac, using an in-house library based on ITK and VTK (Kitware, Clifton Park, NY, USA). The numerical model is composed of a gantry and an imager, both of which can rotate in a rigid fashion around a nominal mechanical isocenter. A radiation source is located inside the gantry head and is rotating with it. Objects can be introduced in the radiation field, either rigidly attached to the moving gantry or at a fixed point near the isocenter. In the simulation, the origin of the couch phantom is positioned on the mechanical isocenter, while the gantry-mounted custom accessory is fixed at the origin of the gantry's coordinate system. The radiation source can be used to project the BBs position on

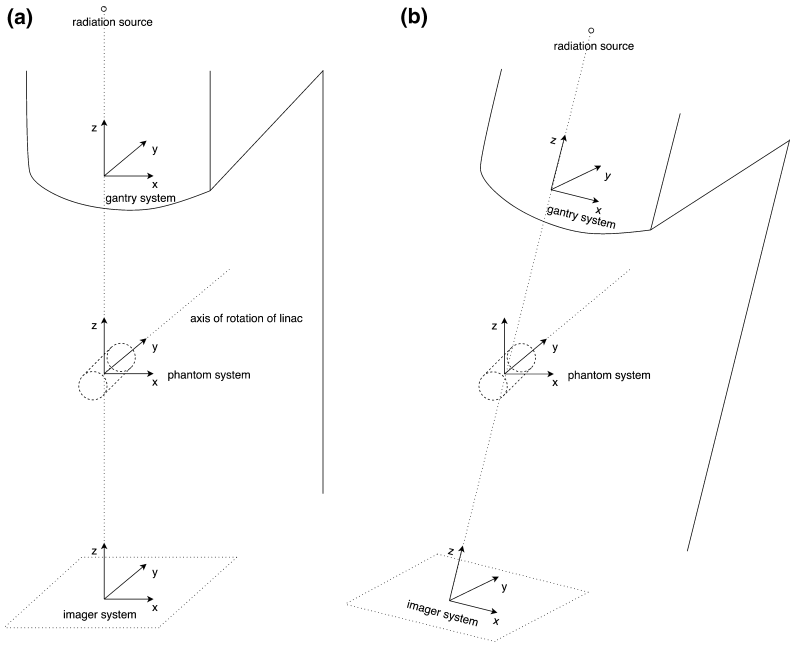

FIG. 1. Coordinate systems used. (a) shows the coordinate sytems at gantry angle 0°, while (b) shows the coordinate systems following a gantry rotation. The axis of rotation of the gantry is around the *Y* axis of the phantom system, which means that only the *X* and *Z* axes of the gantry and imager systems change if the gantry is rotated.

the imager plane, using simple ray tracing to form a simulated EPID image. The BBs positions on the simulated image can then be compared with those measured on the EPID image. Figure 1 presents the coordinate systems used to represent a rigidly rotating gantry and imager, in a phantom-centric coordinate system. When the gantry angle is 0°, the *Z* axis of every coordinate system are aligned. To account for mechanical deformations, both the gantry and imager can be rigidly translated or rotated along the three orthonormal directions of their coordinate system, for a total of 12 DOF. Translation and rotation of the imager will change the position on the EPID of BBs of both the couch phantom and the gantry-mounted accessory. Meanwhile, translation and rotation of the gantry will only affect the position on the EPID of BBs of the gantry-mounted accessory by modifying their position and angle relative to the radiation source and imager. In addition, the source can also move in the *X* and *Y* direction in the nominal coordinate system of the gantry (negative *Z* direction being towards the isocenter). Translation of the source modifies the imaging geometry for both the couch phantom and the gantry-mounted accessory. The source rotates rigidly with the gantry to initialize a given gantry angle, after which source movement and gantry deformations are managed independently. However, the distance between the source and the origin of the gantry system is fixed at the nominal distance between the radiation source and the interface mount (574.4 mm). This amounts to a total of 14 DOF for the whole system (6 for the gantry, 6 for the imager and 2 for the source), and variation of any of these parameters will affect the look of the simulated EPID image. Each degree of freedom will be identified by the following nomenclature: δX denotes a translation along the X axis and ϕX a rotation. Additionally, the coordinate system will be identified in subscript with the indices i (imager), g (gantry) and s (source). For example, δZ_i represent the imager translation along the *Z* axis. Additionally, $\delta\theta$ shall be used to express gantry angular offset from the programmed gantry angle. Finally, the rotations can be expressed in the commonly used pitch, yaw and roll paradigm. ϕZ would then be the skewness or yaw, while ϕX and ϕY refer to pitch and roll, respectively. A particular instance of this modeling class is referred to as a representation of the linac. A representation possesses its own set of mechanical deformations and can simulate an EPID image at any gantry angle. All representations share the same couch and gantry phantoms.

2.B. Optimization

Characterizing the mechanical deformations of a linac is posed as an inverse problem: instead of measuring them directly, mechanical deformations of a representation are optimized to minimize the difference between the measured positions of the BBs on the image and the calculated positions.

The optimization of the deformation parameters is twofold. First, a custom C++ implementation of a elitist genetic algorithm is used on a small, randomly initialized population of representations to find a near-optimal set of deformation parameters. Then, because convergence of the genetic algorithm is slow and not guaranteed, a local optimizer using gradient descent is applied to the intermediary solution. Using only gradient descent seeded at a random seeding point or at the point of no deformations does not converge on the global minimum in most cases, justifying the use of a two-stage

approach. The range of the mechanical deformations is bounded to 16 mm for the translations and 8° for the rotations. The range is high to account for phantom mispositioning. Therefore, it is required that the phantom be aligned within 16 mm of the mechanical isocenter. This range can be increased at the cost of speed if this requirement is too strict. The optimization target, also called fitness in the case of a genetic algorithm, is defined in Eq. (1), in which D_1 to D_n denotes the distance between the measured and simulated BBs center on the imager, n being the quantity of objects being imaged (BBs).

$$F = \sqrt{\sum_{i=1}^{n} D_i^2} \tag{1}$$

2.C. Phantom modeling

In order for the simulator to accurately represent the physical system, the position of the center of BBs in both the gantry accessory and the couch phantom should be known with precision. The couch phantom was scanned using a CT with a $0.5 \times 0.5 \times 1$ mm^3 voxel size. The center of each BB was measured in 2D in the XY, XZ and YZ planes on a thresholded image using CHT and center of mass (CoM). Uncertainties on these measurements were estimated using the standard deviation of the position of the same ball on the associated plane. Measurements from CHT and CoM were then combined using inverse-variance weighted averaging in order to minimize the uncertainty on all BBs position. Two scans were made of the phantom and the final positions measured using the aforementionned method were averaged. The origin of the phantom system is taken as the center of mass of all the BBs. Therefore, it is not directly equivalent to the position of the grooves on the phantom that are used as reference for the room lasers, even though the phantom design makes it so that these two positions are very near. If the lasers were accurately positioned on the origin of the phantom's coordinate system, the calculated position of the mechanical and radiation isocenter would be expressed in the laser's coordinate system, which would be convenient for linac quality assurance.

The positions of BBs in the accessory were measured using the portal imager at 3 collimator angles (0, 90, 270°). The center of each BB was then extracted in 2D using CHT, and backprojected to the interface mount level. The BBs positions at different collimator angles are used to identify the center of rotation of the collimator. Chi-squared analysis is used to identify the point around which a rigid rotation would best explain the measured BBs positions for all collimator angles. This point is taken as the origin of the gantry system presented in Fig. 1. The BBs are assumed to be coplanar, and this hypothesis should hold in the approximation of small source translations.

2.D. Theoretical framework

The solution found by the optimizer is initially expressed in the phantom's coordinate system. This solution must therefore be transformed into the room's coordinate system in order to exclude the effects of improper phantom positioning. It is to be noted that the origin of the room's coordinate system is not the intersection of the actual room lasers, but rather the location of the mechanical isocenter in the simulation. The following equations transform the deformations, expressed in the phantom's coordinate system, into the room's coordinate system by calculating phantom translations and rotations. The position of the resulting mechanical isocenter is an average position for all gantry angles. Phantom translations and rotations can't be known from a single image, but they are constant on every measurements. Thus, they can be extracted by comparing the entire set of images. The small angles approximation was used for these calculations because the rotations of the phantom can be kept small with minimal effort.

2.D.1. Phantom offset

Because the simulation is performed in the phantom's coordinate system, phantom offset from the mechanical isocenter will result in a translation of every other element (imager, gantry and source) in the opposite direction. Thus, it is possible to estimate the phantom offset by averaging the deformations of the gantry, imager and source along each axis. In addition, because the phantom offset is constant in every image, its effect can be averaged over all images. However, because the deformations are measured in the imager and gantry coordinate systems, they must be rotated to express them in room coordinates. Hence, we can express the desired transformations in the following way:

$$O_x = \frac{\sum_{k=1}^{n} (\delta\bar{X}_k cos(\theta_k) + \delta\bar{Z}_k sin(\theta_k))}{n} \tag{2}$$

$$O_z = \frac{\sum_{k=1}^{n} (\delta\bar{Z}_k cos(\theta_k) - \delta\bar{X}_k sin(\theta_k))}{n} \tag{3}$$

$$O_y = \frac{\sum_{k=1}^{n} \delta\bar{Y}_k}{n} \tag{4}$$

where $\delta\bar{X}_k$, $\delta\bar{Y}_k$ and $\delta\bar{Z}_k$ are the average translations of image k for the imager, gantry and source, θ_k is the gantry angle of image k and n is the total number of images used for averaging. It is to be noted that Z is averaged only for the gantry and imager translations because the Z coordinate of the source is assumed to be fixed in the model. The (O_x, O_y, O_z) vector is the translation vector to be applied to the phantom to align it on the mechanical isocenter. Once determined, its effect can be subtracted from the measured deformations on the individual images by using the inverse transform.

2.D.2. Gantry angular offsets

The gantry angular offset represents a difference between the nominal gantry angle and the real gantry angle. The gantry angular offset is expressed by a X translation (in the rotating system) of every element in proportion to its distance to

the isocenter. In addition, it contributes to the Y rotation of the imager and the gantry. Because X translations are also affected by phantom offset, it is clear that gantry angular offsets can't be determined prior to the phantom offset. The angular offset is specific to each gantry angle and can be calculated using the formula:

$$\delta\theta = \frac{\delta X_g/D_g + \delta X_s/D_s + \delta X_i/D_i}{3} \quad (5)$$

where δX_g, δX_s and δX_i denotes the X deformation in their respective coordinate system and D_g, D_s and D_i stands for the nominal distance between the origin of their respective coordinate system and the mechanical isocenter. As discussed previously, angular offsets calculation requires a knowledge of the phantom offset, but phantom offset also will be more precise in the absence of angular offset. Indeed, increased uncertainty results if there is a potential error on the nominal θ or the $\delta\bar{X}$ measurement in formulas (2) to (4). To account for this, phantom offset is first estimated without angular offset. This estimated offset is used to calculate and correct angular offsets, and then phantom offset is calculated again and its effects are subtracted. One iteration of this method is sufficient to obtain high accuracy on both the phantom offset and the angular offset (see Fig. 4 and Section 3.E).

2.D.3. Phantom rotations

Phantom rotations are typically very small since the couch phantom can be aligned with the room lasers using the inlaid grooves. However, even a small rotation can have an effect on the measured deformations. The phantom can be rotated around every axis, but since the Y rotations cannot be distinguished from a gantry angular offset, the rotations to correct are those around Z or X (Φ_Z and Φ_X). Those rotations will have an impact on the measured Y translations (δY), and X and Z rotations (ϕX and ϕZ). The following formulas describe the effect of phantom rotations on those deformations. D represents the nominal distance between the mechanical isocenter and the origin of the coordinate system being corrected.

$$\delta Y = \Phi_X * D * cos(\theta) - \Phi_Z * D * sin(\theta) \quad (6)$$

$$\phi X = \Phi_X * cos(\theta) - \Phi_Z * sin(\theta) \quad (7)$$

$$\phi Z = \Phi_X * sin(\theta) + \Phi_Z * cos(\theta) \quad (8)$$

In order to correct for phantom rotations, we calculate the deformations on every image and then do a regression of Eqs. (6)–(8) to obtain averages for Φ_X and Φ_Z and subtract their effects.

2.E. Radiation and mechanical isocenter

The radiation isocenter is usually defined by the smallest sphere touching every radiation central ray.[8] Thus, both its position and its radius are of interest. Radiation central ray is taken to be the line originating at the radiation source and passing through the middle of the collimation. The position of the radiation isocenter is found iteratively by an algorithm calculating the shortest distance from a point to every radiation central ray and subsequently moving this point in the direction of the farthest ray. The algorithm converges to the radiation isocenter and the radius of the radiation isocenter sphere will be the distance from this point to the farthest radiation central ray. This algorithm is a variation of the gradient-based search commonly used to solve this problem.[9,10]

On the other hand, the mechanical isocenter is generally defined as the intersection of the axis of rotation of the collimator with the axis of rotation of the gantry. In this work, the mechanical isocenter is defined as the origin of the room's coordinate system, because that is the nominal point around which the imager and the gantry rotate in the simulation. The position of the mechanical isocenter can be found by translating the phantom by the phantom offset correction calculated previously.

3. RESULTS

3.A. Noise and uncertainty

There are two main sources of errors in this method: measurement noise and model errors. Measurement noise is the uncertainty in the determination of the BBs center with CHT. This uncertainty has been reported to be around 0.02 mm[11] for a pixel size of 0.5 mm. In contrast, model errors arise from uncertainties in the identification of the BBs positions after CT scanning the phantom. Both types of errors can be simulated by adding gaussian noise in the result of the ray-tracing or in the ball bearings' position in the phantom model. These sources of errors increase the uncertainty on the mechanical deformations measured. Relationships between noise in the model, fitness and uncertainties on the mechanical deformations are studied through simulation. The experimental setup is simulated by generating an image of the phantom and accessory, and adding the constant detection noise on the BBs positions. Then, another simulator in which the phantom and accessory contain variable gaussian noise is used to optimize the deformations in order to reproduce the simulated image. The noise added to the phantom is twice larger along the Y axis because it is the low resolution axis of the original CT scans of the phantom. The noise added to the X and Y axes of the accessory was half of that added to the X axis of the phantom, because the distance from the accessory to the source is approximately half that of the phantom to the source. A 0.5 mm error at the accessory level becomes approximately a 1 mm error at the phantom level. Simulations were carried out 480 times at each level of noise to limit statiscal error. Figure 2 shows how model errors affect the fitness of the resulting solution. The linear relationship between these two parameters breaks down at low model errors, when the measurement noise on the image becomes greater than the error in the model. From the mean fitness of our measurements (0.475 mm), we can interpolate on Fig. 2 the level of noise in our phantom model, which yields a 0.05 mm

standard deviation of noise in X and Z axis, and a 0.10 mm in the Y axis. It also means a 0.025 mm mean error for BBs in the gantry accessory in the X and Y directions.

Of particular importance is the relationship between a given level of fitness and the uncertainty associated with the deformations calculated. Figure 3 shows that the average uncertainty associated with the deformation increases linearly with fitness. So, low fitness is directly linked to precise measurements of the deformations. Interpolating on Fig. 3 yields a mean error of 0.15 mm or 0.15°. It is also useful to know the uncertainty on each deformation parameters given a specific noise level, as shown in Fig. 4. As expected, the

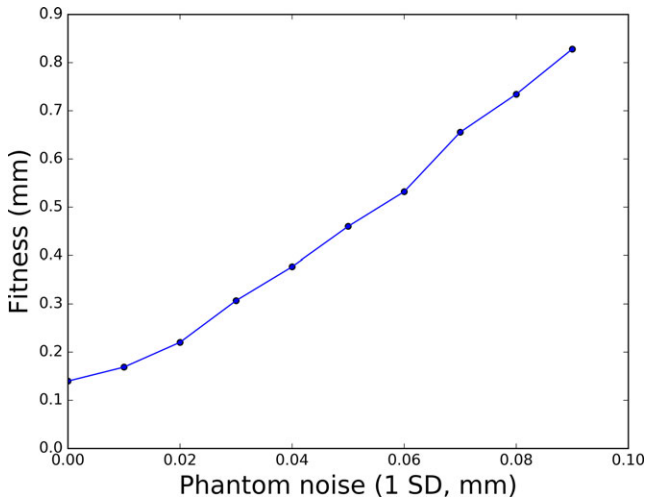

FIG. 2. Relationship between fitness and level of noise in the phantom. Noise level reported is the one along the X and Z axis of the phantom. The fitness increases linearly with increasing noise, but the relationship breaks down at low noise levels, when the CHT measurement noise becomes greater than the modeling errors in the phantom and the accessory.

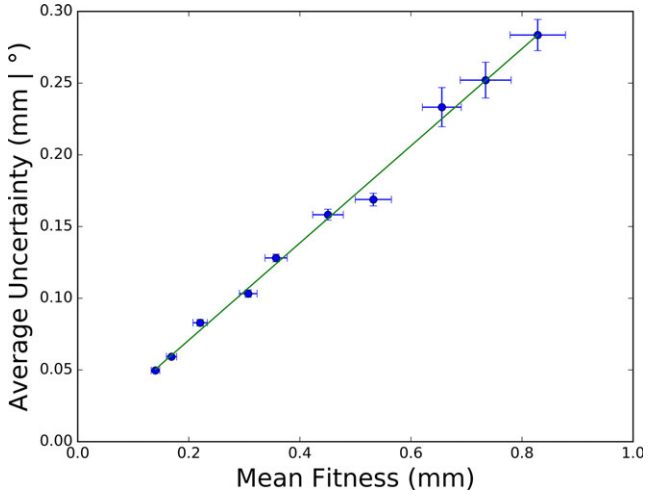

FIG. 3. Relationship between mean uncertainty and fitness. Mean uncertainty on the mechanical deformations increases linearly with fitness. As such, limiting model errors will linearly improve the uncertainty on the mechanical deformations.

parameters that cause the smallest changes in the image are those with the highest uncertainty, for example X and Y rotations and Z translations. It is to be noted that this uncertainty is mostly due to errors in the phantom model, which are the same every time. Therefore, even though the actual value may differ from the measured one, the error on the difference of two measurements is much smaller. In order to compare the performances of our method, uncertainties were calculated for the situation where only 8 DOF are used (6 DOF for the imager, 2 DOF for the source) for the same noise level in the phantom (0.05 mm). In this situation, no gantry-mounted accessory is used. The uncertainties for the 8 DOF method are all higher than the 14 DOF method, except for the X translation of the imager.

3.B. Testing and reproducibility

Figure 5 illustrates the success of the optimized simulator to reproduce the positions of the BBs on the EPID image. The fitness of this solution is 0.489 mm, which, according to Eq. (1), means an average error of 0.086 mm between the simulated and measured centers of the ball bearings at isocenter level, less than 0.4 pixels when the imager is at 1500 mm SDD.

In order to verify the reproducibility of the measurements, 2 measurement sessions spaced 3 weeks apart on the same accelerator took place. No mechanical adjustments were made to the linac during this period. The results are shown in Fig. 6. During each session, the test was executed twice: first, to establish the baseline deformations (shown as continuous lines), and then to detect introduced errors (dotted lines). The introduced errors for the first measurements were a 0.3° gantry angular error at each gantry angle (blue curve) that was introduced by executing the same plan, but with all programmed angles differing by 0.3°. A 1 mm phantom offset along every axis was introduced using table movements. Then, a 0.27 mm source displacement in X was introduced for the second set of measurements. The source displacement was relative to the source position in the first test execution. It was introduced by modifying the source position on the target using the linac beam steering and adjusting the beam steering servos, and the amplitude of the source displacement was measured with the independent verification method presented in Chojnowski et al.,[12] but with a manually positionned ionisation chamber. Table I presents the averages of errors detected at each gantry angle. The uncertainty is the standard deviation of these measured errors, except for the phantom offset where the uncertainty is the expected error established by simulation. The reported value is the average error (±1 SD) detected over the gantry rotation (except for the phantom offset, whose error is the expected error established by simulation). The error reported is lower than the average uncertainty because the parameters tested were expected to be well detected according to the uncertainty analysis for $\delta\theta$, δX_s (see Fig. 4). The experimental standard deviation was very similar to the one predicted in simulation (0.02° compared to 0.01° in simulations for the gantry angular offset and

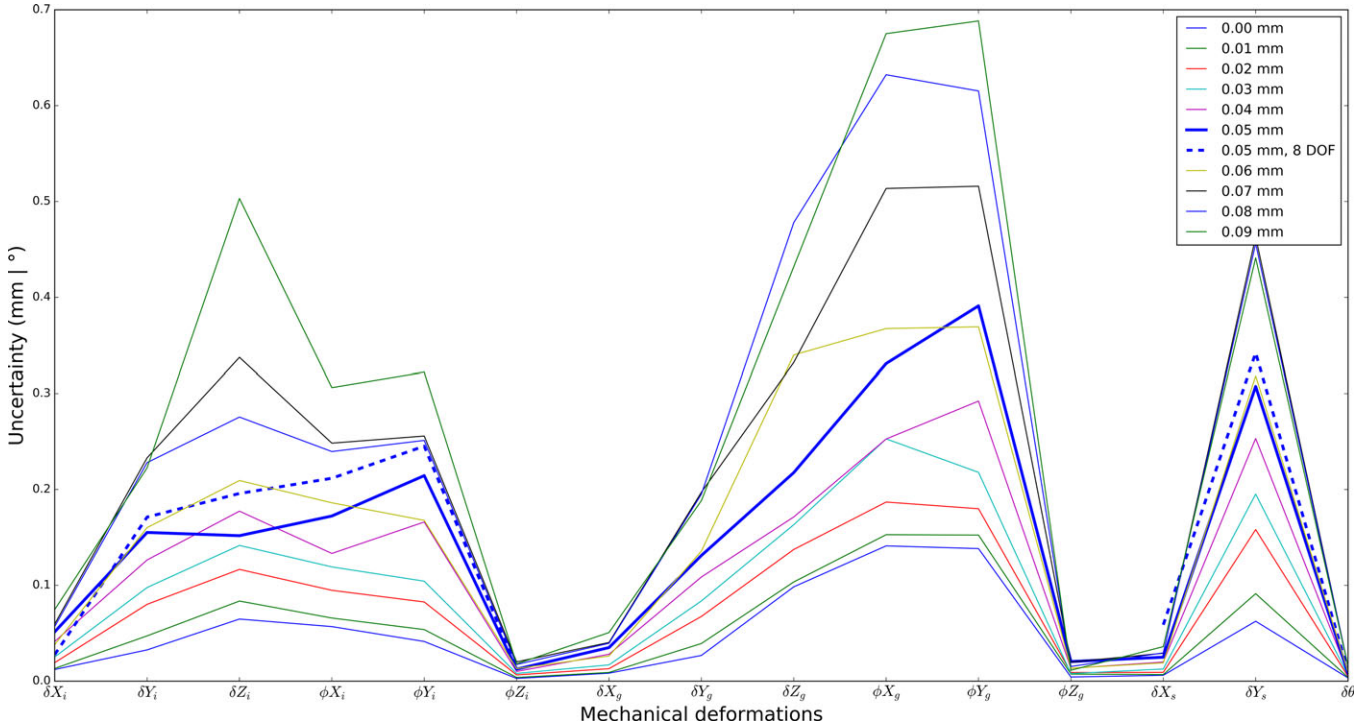

FIG. 4. Uncertainty associated with each degree of freedom for different levels of noise. $\delta Z_{i,g}$, $\phi X_{i,g}$, $\phi Y_{i,g}$ and δY_s are the degrees of freedom showing the largest uncertainties. The thick blue line represents the curve that is the closest to the expected noise level in the phantom (0.05 mm). As a comparison, the dashed line is the curve for the formulation of the problem using only the couch phantom and 8 DOF (6 DOF for the imager, 2 DOF for the source) for the same noise level in the phantom (0.05 mm).

0.02 mm compared to 0.03 mm in simulations for X translation of the source). Furthermore, Fig. 6 shows that the mechanical deformations are quite stable despite the different phantom positioning, which means that the corrections applied for phantom rotations and offset are accurate and that the deformations are reproductible. Although the deformation patterns in δX look sinusoidal, which could indicate a phantom offset, it is to be noted that it is compensated by an opposite pattern in δZ_i, suggesting that the phantom offset found was the best fit possible. Also, the measured mechanical deformations are stable for different setups, which suggests that the pattern is not due to phantom mispositioning. X and Y rotations of both the imager and gantry are relatively stable but show very noisy patterns, which suggests that these deformations are very small and dominated by noise.

3.C. Coupling between DOF

Considering that the current method simultaneously optimizes all mechanical deformations, results will differ from a method using sequential measurements because of coupling between the degrees of freedom. To estimate the amount of coupling between parameters, the optimization algorithm was used sequentially, with each run having control over a few parameters and keeping the others fixed at 0. The optimization was separated in 4 steps: optimization of every X and Y translations, then of Z translations, followed by Z rotations and finally X and Y rotations. The results were then pieced together and corrected for phantom offset and rotations. The results are shown in Fig. 7. The mean fitness of these final results was 1.92 mm, about 4 times worse than when the optimization had control over all parameters at once. However, it seems that coupling is relatively low for X and Y translations, and Z rotations, which are the most useful deformations. X and Y rotations, on the other hand, take very different values. Therefore, sequential measurement on the image should yield good results when measuring translations and Z rotations, but X and Y rotations have too much coupling to do so.

3.D. Contribution of rotations to the solution

Figure 8 shows deformations when X and Y rotations are disabled during the optimization. We see almost no difference in the other mechanical deformations, which furthers the point that these rotations are very small and have little impact on the other parameters. The mean fitness of the solution goes up, which means that the results are generally worse. Since the inclusion of the X and Y rotations seems to have little effects on the other deformations, but tend to drive the fitness down, they can be considered at the optimization despite the larger uncertainties attached to them.

3.E. Radiation Isocenter determination

The determined radiation isocenter can be visualized in Fig. 9. The radius of the radiation isocenter was measured as

0.35 mm, which is in agreement with the star-shot measurements done on this machine. Its position is located at 0.231 mm from the mechanical isocenter, which is better than the 1 mm proposed by TG 142.[1]

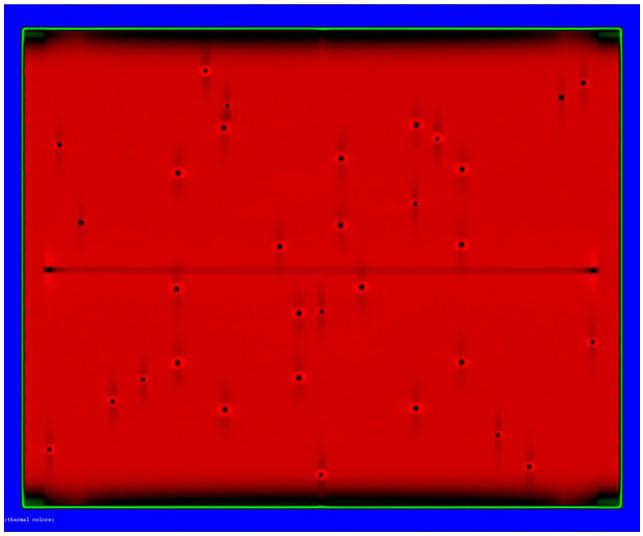

FIG. 5. Optimized simulated image normalized by post-processed image at a gantry and collimator angle of 0°. The small black dots are the simulated positions of the BBs, while the bigger and paler halos around them are the balls' shadow on the imager. Average error between the centers of the simulated and measured BBs is 0.086 mm. The darker streaks in the inplane direction are due to the image pre-processing that included anisotropic gaussian blurring.

4. DISCUSSION

A new method for complete mechanical QA of the linac and isocenter coincidence check has been presented and demonstrated. It can account for more DOF than other published methods and performs a simultaneous rather than sequential characterization of the mechanical deformations. The proposed method is reproductible and easy to use to ensure a complete and precise mechanical QA of the linac. The method is divided in 3 principal steps: measurements, simulation and analysis. First, the BBs positions are measured on every pre-processed EPID images using CHT. Then, using a randomly generated population of simulators using the same phantoms, a genetic algorithm paired with a local optimizer minimizes the difference between the measured and the simulated positions of the BBs. Finally, corrections are applied for phantom offsets, rotations and gantry angular offset. Radiation isocenter position and size is found by gradient descent, using the information from the source position and the measurement of the center of collimation. It combines many different tests into one, improving speed and eliminating experimental setup differences. Linac mechanical deformations, sources movements, phantom positioning, radiation and mechanical isocenter positions are all simultaneously measured in a test procedure taking less than 10 min of linac time and 3 min of analysis. The method doesn't require a complex apparatus nor does it require precise alignment. The method has demonstrated submillimeter accuracy of the mechanical deformations through both simulation and

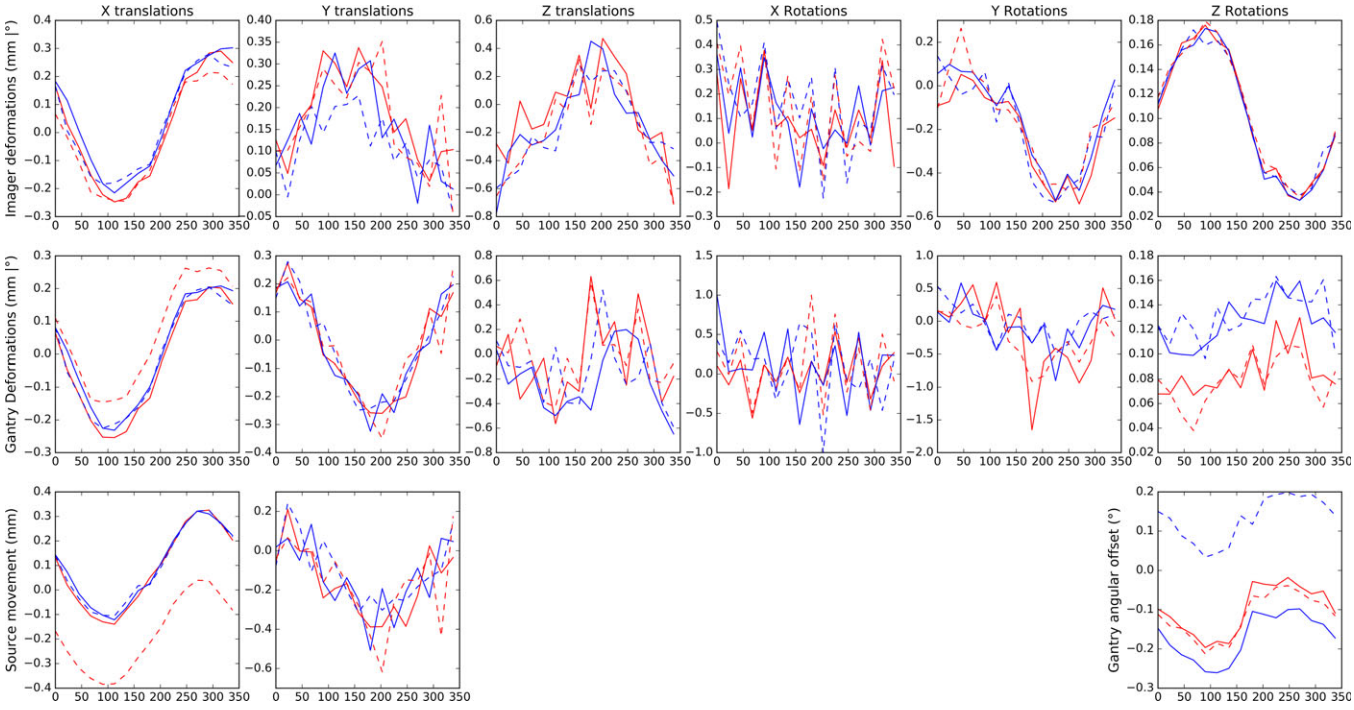

FIG. 6. Mechanical deformations as a function of gantry angle. The blue and red lines represent acquisitions spaced 3 weeks apart. The continuous lines are results for the test executed in normal conditions, while the dotted lines are results in which known errors were introduced in the setup (0.3° angular gantry offset for the dotted blue results and 0.27 mm source movement in *X* for the dotted red results). These errors are well captured in the differences between the angular offsets of the blue curves (0.30 ± 0.02°) and the source movement in *X* of the red curves (0.27 ± 0.02 mm). Deformations are stable and generally under one millimeter or degree.

measurements. The proposed method does not pose requirements on the mechanical behaviour of the investigated linac. The method assumes that the gantry, imager and source follow a perfect, rigid, circular trajectory and any deviation from this motion will be identified. It could be used to measure and monitor a large variety of linac conditions such as rotational hysteresis, by performing the test clockwise and counterclockwise. Although Varian's IsoCal phantom was used in this work, any custom-made phantom without BBs overlaps could be used, as long as a precise model of the BBs positions is available.

Potential improvements could be made to the simplicity of the method by considering the phantom position as additional DOFs during the optimization, eliminating the need for the correction formulas presented in this work. Furthermore, reducing the errors in the phantom model could lead to more accurate measurements of the *X* and *Y* rotations of the gantry and imager, because the magnitude of the mechanical deformations is smaller than the uncertainty on those measurements. Different phantom designs might also help achieve better results by constraining the optimization problem. For instance, a rigid 3D phantom for the interface mount should improve the precision on the *X* and *Y* rotations by amplifying their impact on the image. In order to improve interpretability of the results, further work is required to suggest possible diagnostics to the physicist when the mechanical deformations deviate from the baseline.

TABLE I. Comparison between the measured and introduced errors.

Error type	Introduced value	Measured value
Phantom offset in X (O_x, mm)	1.0 ± 0.1	0.95 ± 0.04
Phantom offset in Y (O_y, mm)	1.0 ± 0.1	1.08 ± 0.04
Phantom offset in Z (O_z, mm)	1.0 ± 0.1	0.91 ± 0.04
Gantry angular offset (δθ, °)	0.30	0.30 ± 0.02
Source movement in X (δX_s, mm)	0.27 ± 0.05	0.27 ± 0.02

4.A. Comparison with other methods

Previously published methods of measuring mechanical deformations involved direct, sequential measurements on the image. Therefore, in some methods, some amount of coupling between the measured deformations is expected. For instance, simple geometrical formulas like those obtained by Rowshanfarzad[2] are only exact when all other deformations are 0, and therefore do not capture the complex interplay that different deformations can have on the image. However, since the measured deformations are small, this hypothesis is reasonable. The measured deformations stay within the range reported by Rowshanfarzad et al.[2] for the translations and *Z* rotation. This is in agreement with Fig. 7, which has shown that the error associated with the sequential measurements of the deformations on the EPID image is small for these degrees of freedom. Coupling analysis also showed that sequential measurement of the *X* and *Y* rotations is quite unreliable. However, our method still exhibits large uncertainty in regards with those degrees of freedom. The method presented by Mao et al.[3,4] also features a simultaneous optimization scheme in a 8 DOF approach. As was shown in Fig. 4, the performances of the 8 DOF approach at the same level of phantom noise are

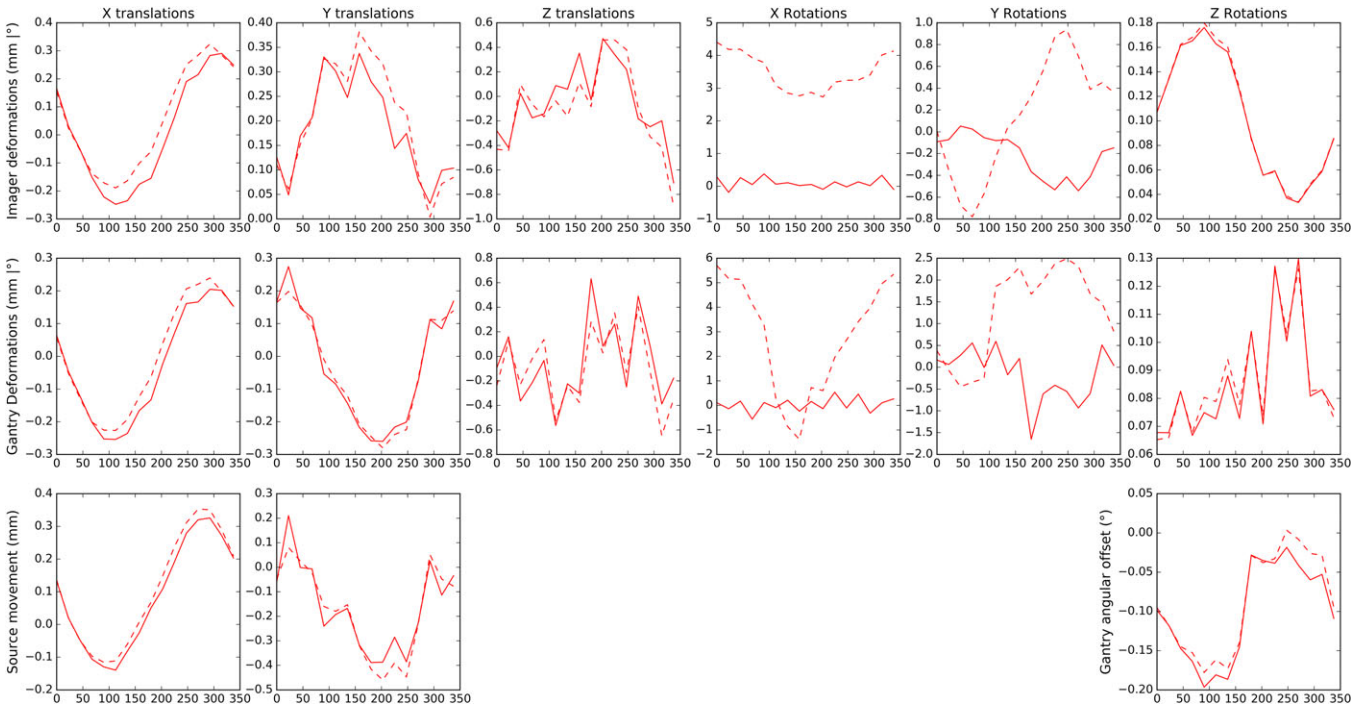

FIG. 7. Coupling analysis of the mechanical deformations. The full line stands for the measurements at collimator angle 0°. The dotted line stands for those same measurements, but optimized sequentially in 4 steps. Most mechanical deformations are well reproduced, but *X* and *Y* rotations differ very significantly. As such, sequential measurements of *X* and *Y* rotations is not recommended.

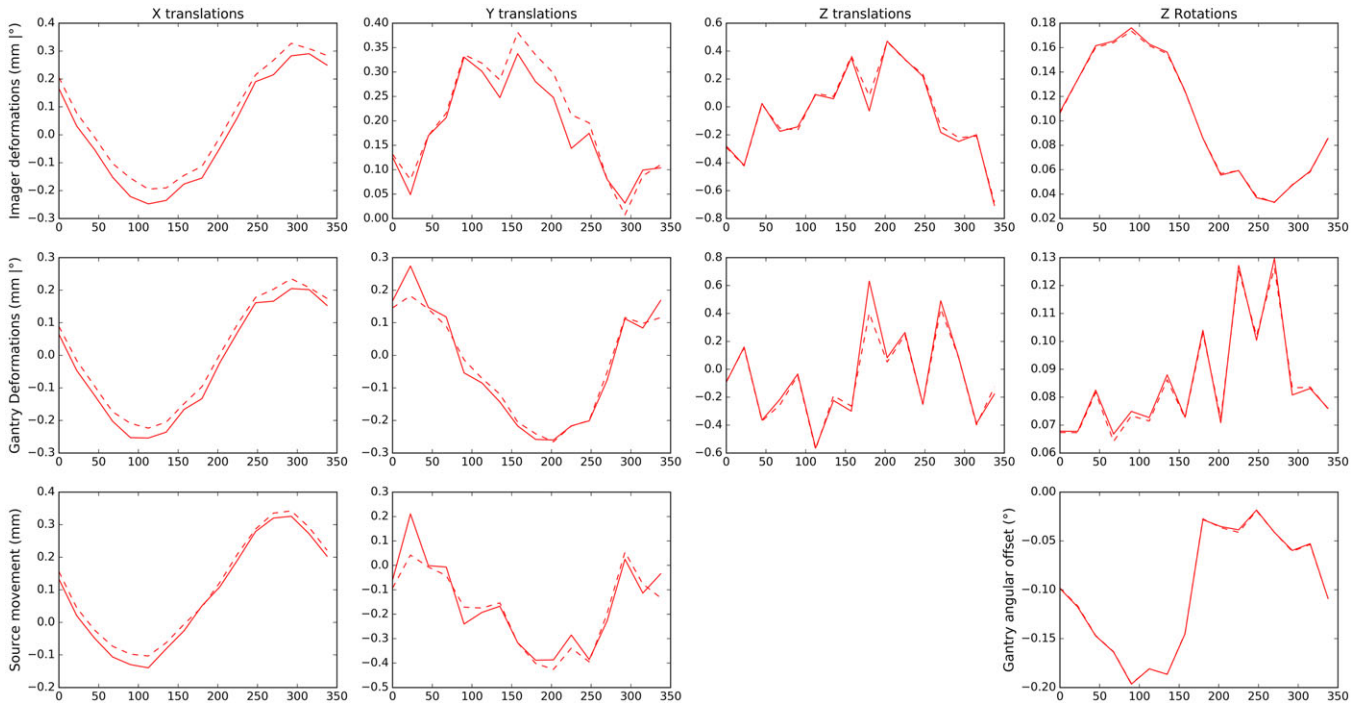

FIG. 8. Mechanical deformations with rotations disabled. The continuous and dotted lines represent the same measurements but the results of the dotted line were optimized with *X* and *Y* rotations set to 0. Little differences can be observed between the curves, but they are very similar. As such, optimizing the rotations will give additional information and improve fitness without affecting adversely the other deformations.

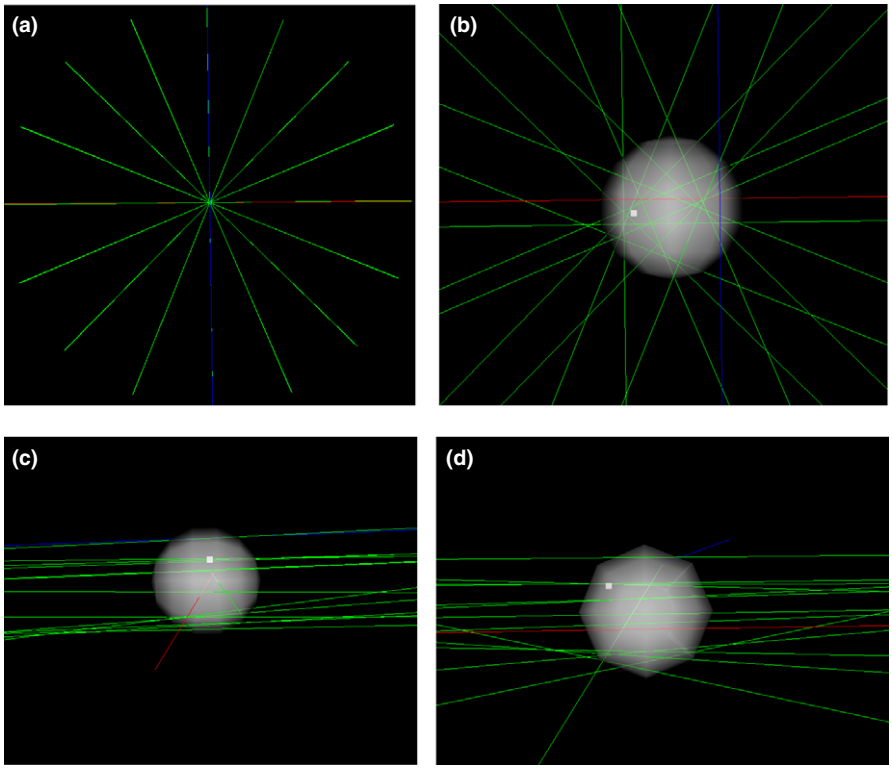

FIG. 9. Radiation central rays and radiation isocenter. (a) Radiation central rays as seen from the viewpoint of an observer standing at the end of the treatment table and looking at the gantry. (b) Close-up view of the radiation isocenter from the same viewpoint as (a). The circle is the radiation isocenter and its radius is 0.35 mm. The white point is the location of the mechanical isocenter. (c) Close-up of the radiation isocenter from the beam's eye-view of gantry angle 180°. (d) Close-up of the radiation isocenter from the beam's eye-view of gantry angle 270°.

lower for all but one of the considered DOF. They report a minimum detectable change in gantry angle of 0.1°, less sensitive than the 0.02° uncertainty on gantry angle obtained with our method. Our method also reports better sensitivity to phantom positional shifts, with a 0.05 mm uncertainty on phantom positioning compared to a maximum difference of 1.6 mm. However, a majority of the precision gains are probably due to the better precision on the phantom model, which they report to be around 0.5 mm, 10 times lower than ours of 0.05 mm. The largest difference is the addition of the gantry's DOF, which enables the monitoring of the collimation and radiation isocenter. In addition, the system's performances and sensitivity to noise are more thoroughly characterized with detailed simulations. Our method represents an improvement over the one used by the IsoCal calibration system[7] because of the additional DOF, especially those related to the source translations. This additional information can be used to extract the radiation central rays and find the position of the radiation isocenter, which can be compared to the mechanical isocenter position in the same referential.

The radiation isocenter radius that was measured is larger than reported by Depuydt et al.[13] for the Varian TrueBeam. However, bigger radii were expected because of the much larger number of central rays considered (16 vs 5). Also, since their method was using films, the isocenter position found was in 2D whereas our method involves 3D determination, which can increase the sphere radius.

In summary, the proposed framework improves upon existing methods by outlining a way to simultaneously measure mechanical and radiation isocenter in the same reference frame and by providing a general method of measuring mechanical deformations including rotations. Uncertainties can be accurately estimated by simulations for any given phantom model, which could lead the design of a 3D gantry accessory to reduce rotational uncertainties.

4.B. Other potential tests using the same phantom & analysis function

Given the very general nature of the analysis method, it can be re-used with minimal adjustments to study other mechanical parameters in the accelerator. For example, if the gantry was stationary, the table could be rotated to a few different angles (avoiding overlaps between accessory and IsoCal phantom BBs) to determine the isocenter of rotation of the treatment table. It could also be used to commission a 6 DOF table, which is now offered by some linac vendors. Indeed, the proposed system is very sensitive to phantom tilts and would be particularly appropriate for the task.

4.C. Generalisation considerations

The test could be generalized to include kV/MV isocenter coincidence check with minimal modifications, since the formalism for the deformations was the same for the kV imaging. The presence of the head mount accessory was not necessary in this scenario since the beam collimation is not of interest. In this case, the problem of CT geometric calibration has already seen complete solutions in the form of 9 DOF calibrations.[14,15] The addition of the kV isocenter verification would use the same setup as the one described in this work, and the resulting images could be analysed with the same software with minimal modifications. However, sequential kV and MV imaging would add time to the QA procedure.

5. CONCLUSION

This work introduces a general approach to linac mechanical QA which caracterizes 14 DOF of the linac, including gantry, imager and source movements. This method can find the position of the mechanical and radiation isocenter in the same coordinate system and is able to produce maps of the mechanical deformations in function of gantry angle. The method's performance were characterized through simulation and tested by introducing known errors into the experimental setup, which were detected with high precision.

ACKNOWLEDGMENTS

D.G. acknowledges partial support by the CREATE Medical Physics Research Training Network grant of the Natural Sciences and Engineering Research Council (Grant number: 432290). The authors have no conflicts of interest to disclose.

[a)]Author to whom correspondence should be addressed. Electronic mail: louis.archambault@ulaval.ca.

REFERENCES

1. Klein EE, Hanley J, Bayouth J, et al. Task group 142 report: quality assurance of medical accelerators). *Med Phys*. 2009;36:4197–4212.
2. Rowshanfarzad P, McGarry CK, Barnes MP, Sabet M, Ebert MA. An EPID-based method for comprehensive verification of gantry, EPID and the MLC carriage positional accuracy in Varian linacs during arc treatments. *Radiat Oncol (London, England)*. 2014;9:249.
3. Mao W, Lee L, Xing L. Development of a QA phantom and automated analysis tool for geometric quality assurance of on-board MV and kV x-ray imaging systems. *Med Phys*. 2008;35:1497–1506.
4. Mao W, Speiser M, Medin P, Papiez L, Solberg T, Xing L. Initial application of a geometric QA tool for integrated MV and kV imaging systems on three image guided radiotherapy systems. *Med Phys*. 2011;38:2335–2341.
5. Chiu TD, Yan Y, Foster R, Mao W. Long-term evaluation and cross-checking of two geometric calibrations of kV and MV imaging systems for Linacs. *J Appl Clin Med Phys*. 2015;16:306–310.
6. Nyiri BJ, Smale JR, Gerig LH. Two self-referencing methods for the measurement of beam spot position. *Med Phys*. 2012;39:7635–7643.
7. Mamalui-Hunter M, Li H, Low DA. Linac mechanic QA using a cylindrical phantom. *Phys Med Biol*. 2008;53:5139.
8. Lutz W, Winston KR, Maleki N. A system for stereotactic radiosurgery with a linear accelerator. *Int J Radiat Oncol Biol Phys*. 1988;14:373–381.
9. Winkler P, Bergmann H, Stuecklschweiger G, Guss H. Introducing a system for automated control of rotation axes, collimator and laser adjustment for a medical linear accelerator. *Phys Med Biol*. 2003;48:1123.

10. Skworcow P, Mills JA, Haas OC, Burnham KJ. A new approach to quantify the mechanical and radiation isocentres of radiotherapy treatment machine gantries. *Phys Med Biol*. 2007;52:7109.
11. Rowshanfarzad P, Sabet M, O'Connor DJ, Greer PB. Isocenter verification for linac-based stereotactic radiation therapy: review of principles and techniques. *J Appl Clin Med Phys*. 2011;12:3645.
12. Chojnowski JM, Barnes MP, Sykes JR, Thwaites DI. Beam focal spot position: the forgotten linac QA parameter. An EPID-based phantomless method for routine Stereotactic linac QA. *J Appl Clin Med Phys*. 2017;18:1526–9914.
13. Depuydt T, Penne R, Verellen D, et al. Computer-aided analysis of star shot films for high-accuracy radiation therapy treatment units. *Phys Med Biol*. 2012;57:2997.
14. Cho Y, Moseley DJ, Siewerdsen JH, Jaffray DA. Accurate technique for complete geometric calibration of cone-beam computed tomography systems. *Med Phys*. 2005;32:968–983.
15. Zechner A, Stock M, Kellner D, et al. Development and first use of a novel cylindrical ball bearing phantom for 9-dof geometric calibrations of flat panel imaging devices used in image-guided ion beam therapy. *Phys Med Biol*. 2016;61:N592.